

See discussions, stats, and author profiles for this publication at: <https://www.researchgate.net/publication/263941845>

Experimental Measurement of the Effective Thermal Conductivity of Ash Deposit for High Sodium Coal (Zhun Dong Coal) in a 300 KW Test Furnace

ARTICLE *in* ENERGY & FUELS · NOVEMBER 2013

Impact Factor: 2.79 · DOI: 10.1021/ef4012017

CITATIONS

13

READS

42

4 AUTHORS, INCLUDING:



Hao Zhou

Zhejiang University

136 PUBLICATIONS 784 CITATIONS

SEE PROFILE

Experimental Measurement of the Effective Thermal Conductivity of Ash Deposit for High Sodium Coal (Zhun Dong Coal) in a 300 KW Test Furnace

Hao Zhou,* Bin Zhou, Letian Li, and Hailong Zhang

Zhejiang University, Institute for Thermal Power Engineering, State Key Laboratory of Clean Energy Utilization, Hangzhou 310027, People's Republic of China

ABSTRACT: This paper presents the measurement of effective heat conductivity of ash deposit based on a novel technique for Zhun Dong coal (ZD) with high sodium in a pilot scale furnace. The variation of deposit thickness with time is determined by digital image technique. In addition, simplified two color method is applied to obtain the deposit surface temperature. Subsequently, the change of the average effective heat conductivity of the ash deposit with deposit growth is calculated by combining the deposit surface temperature and thickness. Meanwhile, mineral phases of the ash deposits were identified by X-ray diffraction spectrometry (XRD); scanning electron microscopy (SEM) was applied to analyze the microstructure of ash deposit, and the corresponding chemical compositions were determined by energy dispersive X-ray spectrometry (EDX). The growth process of the ash deposit on probe 2 was composed of four stages based on digital image technique. This was confirmed by the layer structures of the slagging deposits. In addition, the deposit surface temperature increased with time, and it finally fluctuated around 1255 °C. Meanwhile, the results showed that the average effective heat conductivity of the ash deposit on probe 2 increased linearly with deposit growth. The XRD analysis results of three deposits showed that these deposits had similar mineralogy in every layer structure. The content of gehlenite in the deposit increased with the deposit growth. Moreover, the loss of glass is accompanied by a corresponding increase in crystalline phase.

1. INTRODUCTION

Coal will continue to be the major fossil energy source in next decades in China due to its rich reserves. Nevertheless, there are several issues required to be solved with respect to the application of coal in utility boilers. Characteristics of coal can impact on the overall operation of the power plant boiler, for instance, waste treatment demand, capacity of power generation, equipment failure rate, and generally speaking, it influences the environment.¹ The most important negative impact of coal on industrial boilers are the problems with slagging, fouling, and pollution. The ash deposits not only deteriorate heat transfer ability of water wall tube but also result in corrosion of boiler tubes and flue blockage.² All these phenomena may give rise to reduced efficiency, power generation capacity, system availability, and subsequent increase in the power generating cost.^{2–7}

As is well-known, many physical and chemical processes are involved in the ash deposit formation. It can be affected by many factors, for instance, coal type, furnace temperature, surface temperature of the water wall tube, tube materials, reaction atmosphere, flow dynamics, ash transport mechanisms, and so forth.^{8,9}

During coal combustion, the inorganic components will be transformed into ash species. Tomeczek et al. proposed that ash particles adhere to heat-exchanger tube from the combustion gas principally through two main transport mechanisms (i.e., diffusion and inertial impaction).¹⁰ The inertial impaction was most vital mechanism for large particles ($>10\ \mu\text{m}$) to deposit on tube surface. Whereas, the fine particles ($<10\ \mu\text{m}$) deposition on the tube surface is controlled by turbulent diffusion.

In recent years, the thermal conductivity of ash deposit issue has been focused by some researchers.^{11–14} The reported values

varied from $0.14\ \text{W m}^{-1}\ \text{K}^{-1}$ to $15\ \text{W m}^{-1}\ \text{K}^{-1}$.¹¹ The heat conductivity of ash deposit is mainly affected by three factors, for instance, temperature of the deposit, chemical composition, and physical structure. Nevertheless, a few researches have investigated the actual deposits in pilot scale of pulverized coal combustion furnace. Moreover, the two color method was widely applied in noncontact measurement of flame temperature^{15,16} and soot temperatures.^{17,18} Nevertheless, few researches can determine the surface temperature of the ash deposit in the actual furnace by using the two color method.

The ZD coal applied in this study is one of the most commonly employed low rank coals in Chinese power plant. It is produced from Xinjiang province in China with high levels of sodium, high content of moisture, and large reserves. However, it has resulted in serious fouling and slagging problems in industrial power plants due to its high level of sodium. To date, no systematic investigation reported for ZD coal in the literature, which deals with the heat conductivity of deposit for this coal.

The purpose of this work is to determine the effective heat conductivity of the ash deposit for ZD coal in a 300 KW test furnace through the simplified two color method and digital image technique. In this paper, the deposit thickness is calculated by digital image technique, and the deposit surface temperature is obtained by two color method. The average effective heat conductivity of deposit is calculated by combining the deposit thickness and deposit surface temperature. In addition, XRD

Received: June 27, 2013

Revised: November 4, 2013

Published: November 4, 2013



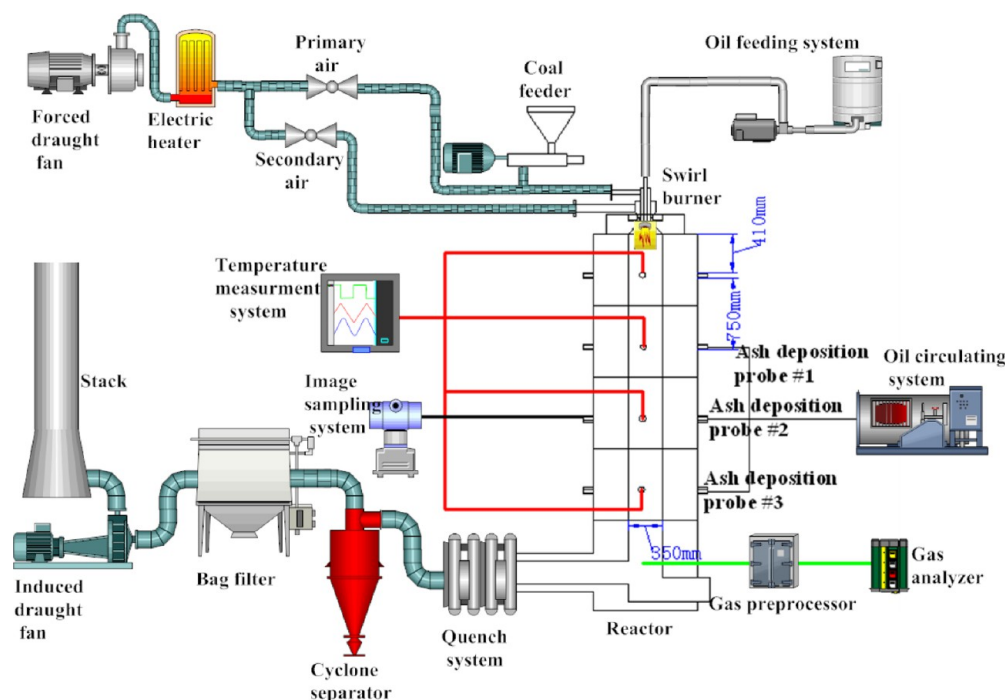


Figure 1. Schematic diagram of the tested furnace^{19,20}

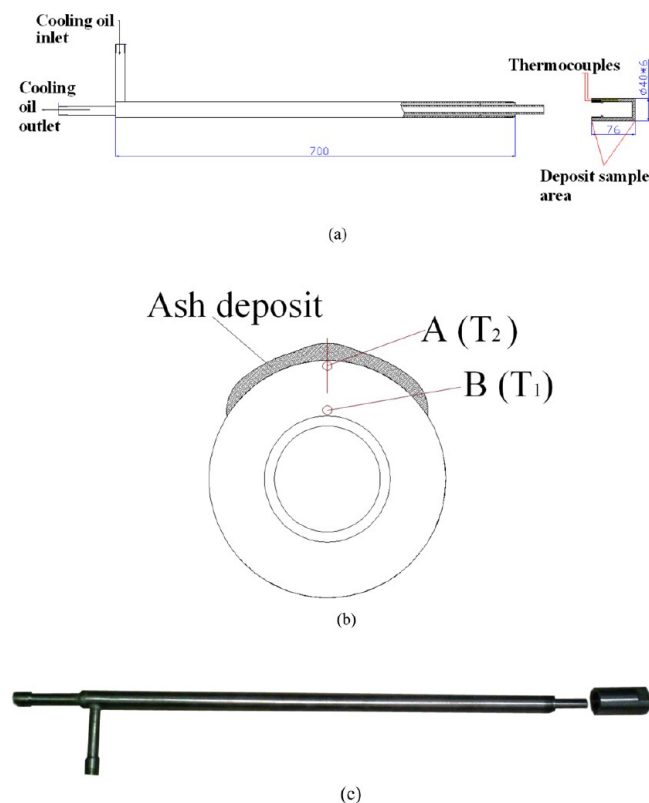


Figure 2. (a) Schematic diagram of deposition probe. (b) Close-up of the deposition sampling part.^{19,20} (c) The detail of deposition sampling part.

is used to identify the mineralogy of ash deposit. The microstructure of ash deposit and the corresponding chemical composition are analyzed by SEM-EDX, which would promote to get insight into the factors effect on the average thermal conductivity of deposit of ZD coal.

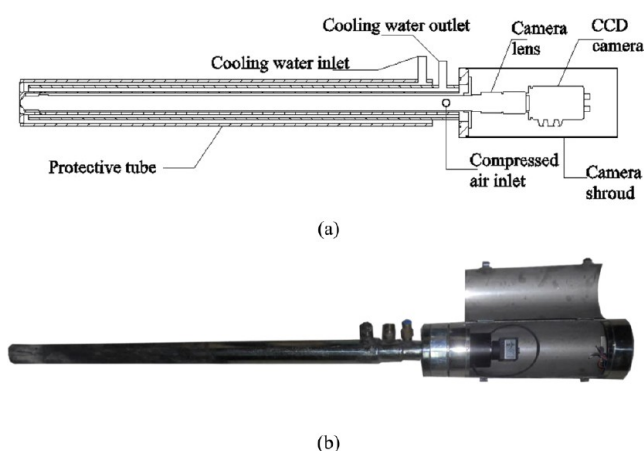


Figure 3. (a) Schematic diagram of CCD monitoring system. (b) The detail of CCD monitoring system detail.^{19,20}

2. EXPERIMENTAL SECTION

2.1. The Furnace. The measurement of effective thermal conductivity of deposit was conducted in a 300 KW pulverized fired furnace, as illustrated in Figure 1.^{19,20} It primarily consists of coal feeder, swirl burner, combustion chamber, image sampling system, temperature measurement system, and ash deposition sampling system. The inner diameter and total height of the combustion chamber are 350 and 3950 mm, respectively. To reduce the heat loss, refractory material is used to mount in the interior of the furnace. When the operation conditions of the furnace reach the required parameters, the coal feeding rate is fixed at 40 kg/h.

Three deposition probes are inserted into the furnace center, and with the burner mutually be apart from 2660, 1910, and 1160 mm, respectively, as illustrated in Figure 1. Meanwhile, the deposit growth is online monitored by the image sampling system. This sampling system is located in the opposite side of the second deposition probe. The furnace temperatures are monitored by S-Type thermocouples. At the outlet of the furnace, the flue gas compositions are analyzed by the flue gas preprocessor and analyzer. In addition, a bag filter is applied to

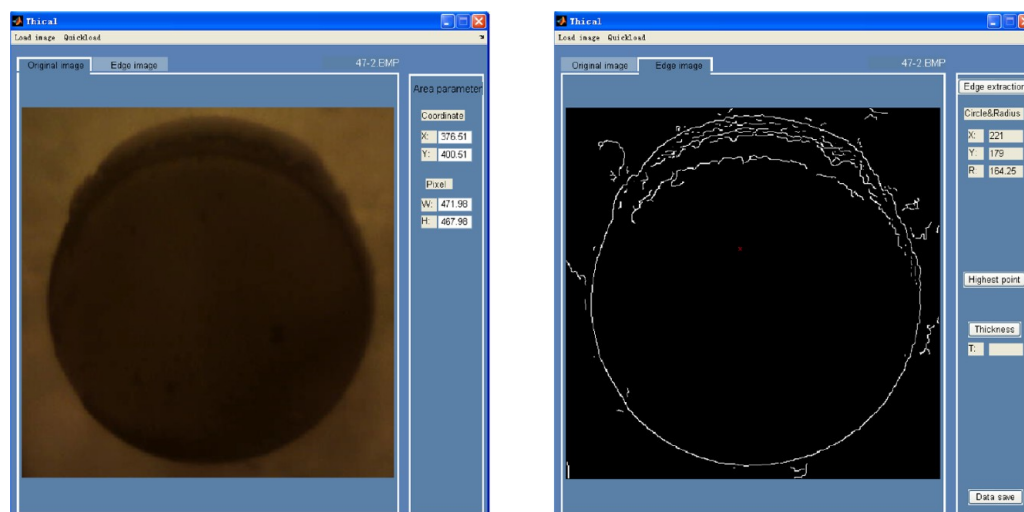


Figure 4. Method of digital image processing; the original image (left) and the edge image (right).

Table 1. Experimental Parameters

| | |
|--|---------|
| coal | ZD |
| thermal load (kW) | 350 |
| excess air ratio | 1.2 |
| air velocity (m/s) | ~2.8 |
| T_{gas} around probe 1 ($^{\circ}\text{C}$) | ~1320 |
| T_{gas} around probe 2 ($^{\circ}\text{C}$) | ~1270 |
| T_{gas} around probe 3 ($^{\circ}\text{C}$) | ~1100 |
| oxygen concentration at outlet of the furnace (%) | 4.0–5.0 |
| duration (min) | 240 |

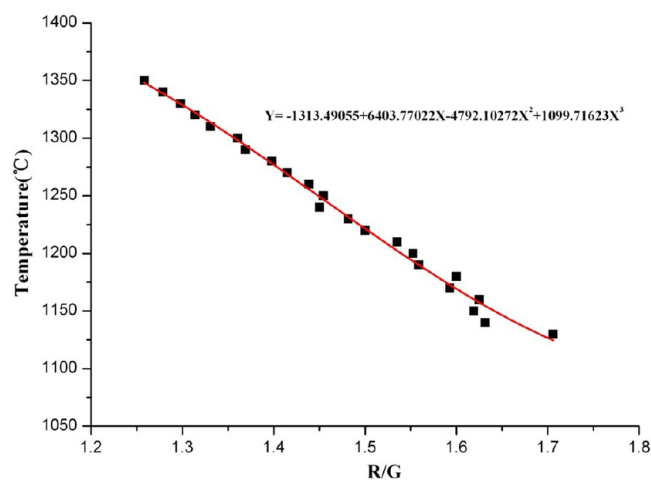


Figure 5. Change of the temperature versus the characteristic data (R/G), and the corresponding polynomial fitting equation.

prevent the fine particles into the atmosphere. In order to prevent the high-temperature flue gas from being discharged into the atmosphere, the heat exchanger system is mounted in the rear flue. Moreover, Table 1 illustrated the corresponding experimental conditions.

2.2. Deposit Sampling System. Once the operation conditions of the test furnace meet the requirement and hold steady, the three deposition probes are inserted in the center of furnace. The probe made of stainless steel principally consists of an oil-cooled tube section and a deposit sampling section. The connection between them is through screw thread (see Figure 2a, b).^{19,20} The outer diameter and length of the deposit sampling part are 40 and 76 mm, respectively. An oil-circulating temperature unit is applied to keep the temperature of cooling oil stable. In this study, the temperature of cooling oil is

Table 2. Red (R), Green (G), and Blue (B) Color Signals (0–255) Obtained by the CCD Camera Monitoring System from the Color Images of a Blackbody Furnace at Different Temperatures, and the Corresponding Characteristic Parameter X_{RG}

| blackbody furnace temp. ($^{\circ}\text{C}$) | red (R) | green (G) | blue (B) | characteristic param. X_{RG} |
|--|---------|-----------|----------|---------------------------------------|
| 1120 | 25 | 14 | 10 | 1.7857 |
| 1130 | 29 | 17 | 11 | 1.7059 |
| 1140 | 31 | 19 | 12 | 1.6316 |
| 1150 | 34 | 21 | 14 | 1.61905 |
| 1160 | 39 | 24 | 15 | 1.6250 |
| 1170 | 43 | 27 | 17 | 1.5926 |
| 1180 | 48 | 30 | 18 | 1.6000 |
| 1190 | 53 | 34 | 21 | 1.5588 |
| 1200 | 59 | 38 | 23 | 1.5526 |
| 1210 | 66 | 43 | 25 | 1.5349 |
| 1220 | 72 | 48 | 28 | 1.5000 |
| 1230 | 80 | 54 | 31 | 1.4815 |
| 1240 | 87 | 60 | 34 | 1.4500 |
| 1250 | 96 | 66 | 38 | 1.4545 |
| 1260 | 105 | 73 | 41 | 1.4384 |
| 1270 | 116 | 82 | 46 | 1.4146 |
| 1280 | 130 | 93 | 52 | 1.3979 |
| 1290 | 141 | 103 | 58 | 1.3689 |
| 1300 | 151 | 111 | 62 | 1.3604 |
| 1310 | 165 | 124 | 69 | 1.3306 |
| 1320 | 180 | 137 | 77 | 1.3139 |
| 1330 | 196 | 151 | 85 | 1.2980 |
| 1340 | 211 | 165 | 93 | 1.2788 |
| 1350 | 229 | 182 | 104 | 1.2582 |

controlled at 503 K. In order to measure the outer and inner surface temperature of the deposition probe, the end surface of the deposit sampling section has been drilled two small holes, as illustrated in Figure 2. During the experiment, two K-type thermocouples are installed in them.

2.3. Image Sampling System and Description of Digital Image Technique. In this work, the ash deposit growth is monitored by a Charge Coupled Device (CCD) monitoring system. Figure 3a, b present the schematic diagram and corresponding detail of the system, respectively.^{19,20} The monitoring system can be divided into four parts: (1) CCD camera; (2) camera lens; (3) protective tube; (4) camera shield. The detailed descriptions of the CCD monitoring system were presented in our previous studies.^{19,20}

Table 3. Comparison of the Set Temperatures with the Calculated Temperatures and the Errors

| temp. of blackbody (°C) | temp. calcd. values (°C) | errors (°C) |
|-------------------------|--------------------------|-------------|
| 1120 | 1102.92 | -17.08 |
| 1130 | 1124.59 | -5.41 |
| 1140 | 1154.40 | 14.4 |
| 1150 | 1160.14 | 10.14 |
| 1160 | 1157.39 | 2.61 |
| 1170 | 1172.82 | 2.82 |
| 1180 | 1169.20 | -10.8 |
| 1190 | 1189.92 | -0.08 |
| 1200 | 1193.15 | -6.85 |
| 1210 | 1202.55 | -7.45 |
| 1220 | 1221.48 | 1.48 |
| 1230 | 1231.70 | 1.7 |
| 1240 | 1249.20 | 9.2 |
| 1250 | 1246.67 | -3.33 |
| 1260 | 1255.68 | -4.32 |
| 1270 | 1268.84 | -1.16 |
| 1280 | 1278.07 | -1.93 |
| 1290 | 1293.71 | 3.71 |
| 1300 | 1298.26 | -1.74 |
| 1310 | 1313.68 | 3.68 |
| 1320 | 1322.08 | 2.08 |
| 1330 | 1329.79 | -0.21 |
| 1340 | 1338.78 | -1.22 |
| 1350 | 1347.93 | -2.07 |

Table 4. Proximate Analysis, Ultimate Analysis, Gross Heating Value, Ash Melting Temperature, and Chemical Composition of ZD Coal

| ZD coal | | |
|-------------------------------|--------------------------------|-------|
| moisture, (wt %, ad) | | 15.6 |
| proximate, (wt %, db) | volatile matter | 32.79 |
| | ash | 12.3 |
| | fixed carbon | 52.91 |
| ultimate analysis, (wt %, db) | carbon | 64.07 |
| | hydrogen | 3.58 |
| | nitrogen | 0.65 |
| | sulfur | 0.18 |
| | oxygen | 19.22 |
| HV (MJ/kg) | HHV | 24.01 |
| Ash melting temperature, (°C) | IT | 1213 |
| | ST | 1218 |
| | HT | 1221 |
| | FT | 1231 |
| ash composition (wt %) | Al ₂ O ₃ | 14.04 |
| | CaO | 27.78 |
| | SiO ₂ | 35.08 |
| | K ₂ O | 0.48 |
| | MgO | 4.73 |
| | Fe ₂ O ₃ | 6.07 |
| | Na ₂ O | 8.31 |
| | TiO ₂ | 0.71 |
| | SO ₂ | 2.80 |

During the experiment, CCD camera is applied to record the deposit growth process. Then, the image processing system was applied to postprocess the recorded video into 24-bit images. Meanwhile, the image processing system calculated the deposit thickness based on the detection of the edge detection and algorithm of Hough transform. The detail principle of the digital image processing system was illustrated in

previous research.^{19,20} The detail of the digital image processing is shown in Figure 4.

2.4. Measurement Principle of Deposit Surface Temperature.

The radiation of a gray body obeys Planck's radiation law:

$$E(\lambda, T) = \varepsilon_{\lambda} \frac{C_1}{\lambda^5 \left[\exp\left(\frac{C_2}{\lambda T}\right) - 1 \right]} \quad (1)$$

where $E(\lambda, T)$ presents the monochromatic radiation power of a gray body ($\text{W m}^{-2} \mu\text{m}^{-1}$), λ represents the radiation wavelength (μm), T denotes absolute temperature (K), C_1 and C_2 are the first and second Planck's constants, and ε_{λ} is monochromatic emissivity. The wavelength range involved in this paper is from 380 to 760 nm (visible light). Due to $C_2/\lambda T \gg 1$, Wien's radiation law can replace Planck's law:¹⁵

$$E(\lambda, T) = \varepsilon_{\lambda} \frac{C_1}{\lambda^5} \exp\left(-\frac{C_2}{\lambda T}\right) \quad (2)$$

Each deposit image frame generated by CCD camera can be decomposed into three dominant color signals red (R), green (G), and blue (B). They can be obtained by the Planck's radiation law, and the corresponding equation is as follows:

$$\begin{cases} R(T) = S_R \varepsilon(\lambda_R, T) \frac{C_1}{\lambda_R^5} \exp\left(-\frac{C_2}{\lambda_R T}\right) \\ G(T) = S_G \varepsilon(\lambda_G, T) \frac{C_1}{\lambda_G^5} \exp\left(-\frac{C_2}{\lambda_G T}\right) \\ B(T) = S_B \varepsilon(\lambda_B, T) \frac{C_1}{\lambda_B^5} \exp\left(-\frac{C_2}{\lambda_B T}\right) \end{cases} \quad (3)$$

where S_R , S_G , and S_B are the apparatus constants influenced by a lot of factors, for instance, observation distance, signal conversion, lens properties, atmosphere, and so forth. $\varepsilon(\lambda_R, T)$, $\varepsilon(\lambda_G, T)$, and $\varepsilon(\lambda_B, T)$ are the red, green, and blue emissivity of the ash deposit, respectively.

In this study, ash deposit in the furnace is assumed as gray body. Consequently, the emissivity and wavelength are independent of each other for the ash deposit, for instance, $\varepsilon(\lambda_R, T) = \varepsilon(T)$, and eq 3 can be expressed as

$$\begin{cases} \varepsilon(T) = \frac{R(T)}{R_b(T)} \\ \varepsilon(T) = \frac{G(T)}{G_b(T)} \\ \varepsilon(T) = \frac{B(T)}{B_b(T)} \end{cases} \quad (4)$$

where R_b , G_b , and B_b denote the three main color signals obtained by the CCD camera processing system from a blackbody as its temperature is known. According to the Planck's law, R_b , G_b , and B_b can be expressed as

$$\begin{cases} R_b(T) = S_R \frac{C_1}{\lambda_R^5} \exp\left(-\frac{C_2}{\lambda_R T}\right) \\ G_b(T) = S_G \frac{C_1}{\lambda_G^5} \exp\left(-\frac{C_2}{\lambda_G T}\right) \\ B_b(T) = S_B \frac{C_1}{\lambda_B^5} \exp\left(-\frac{C_2}{\lambda_B T}\right) \end{cases} \quad (5)$$

These parameters can be obtained easily before experiments in the pilot scale furnace as the CCD monitoring system calibration, and a polynomial function, as in eq 6, can be applied to express the relationship between r_b and T .

$$R_b(T) = \sum_{i=0}^n a_i T_i \quad (6)$$

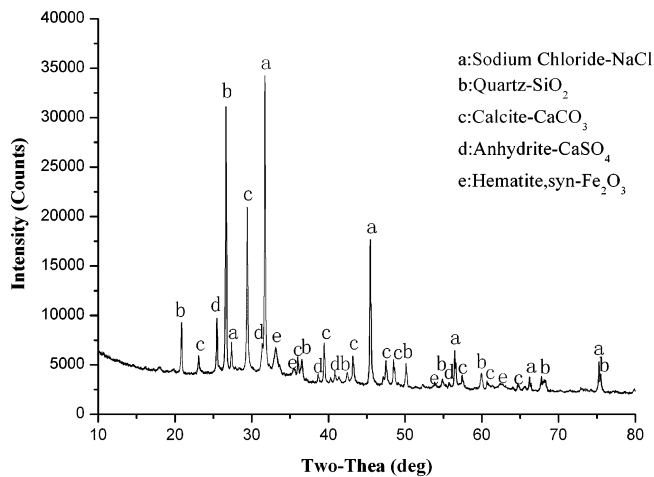


Figure 6. X-ray diffractogram of low-temperature ash (LTA).

Table 5. Mineral Compositions of LTA by XRD (wt % of Crystalline Mineral Matter)

| mineral | LTA |
|--|------|
| quartz (SiO ₂) | 28.0 |
| calcite (CaCO ₃) | 27.6 |
| halite (NaCl) | 24.7 |
| hematite (Fe ₂ O ₃) | 13.4 |
| anhydrite (CaSO ₄) | 6.2 |

The emissivity of ash deposit with a known temperature can be calculated by this equation.

In addition, choosing red and green colors and rearranging eq 4 yields

$$\frac{R(T)}{G(T)} = \frac{R_b(T)}{G_b(T)} = X_{RG}(T) \quad (7)$$

This indicated that the characteristic parameter $X_{RG}(T)$ is identical at the same temperature T . From eq 7, a polynomial function can be applied to fit the relationship between T and $X_{RG}(T)$ as

$$T = \sum_{i=0}^M b_i X_{RG}^i \quad (8)$$

In this study, why the red and green colors have been selected to calculate the temperature of deposit is that CCD camera sensor possesses higher spectral sensitivities to the red and green color signals than to the blue color signal.

The measurement procedure of deposit surface temperature is summarized as follows:

- (1) Obtain color images at different temperatures from a blackbody by the CCD monitoring system at a certain exposure time, and determine polynomial functions of eq 6 and 8.
- (2) Obtain ash deposit images by the CCD monitoring system at the same exposure time, and determine X_{RG} from R and G in the images by eq 7.
- (3) Determine deposit surface temperature T from X_{RG} obtained from the ash deposit images by eq 8.

2.5. Calibration of the CCD Monitoring System. A blackbody furnace is applied to calibrate the CCD monitoring system, and the temperature range of the blackbody furnace is from 773 K to 1873 K with a resolution of ± 1 K. Table 2 shows R, G, and B color signals at different temperatures captured by the CCD monitoring system from the color images of the blackbody furnace. The corresponding exposure time of CCD monitoring system is 7 ms. The characteristic parameter X_{RG} is also shown in Table 2. The variations of temperature (T) with characteristic parameter X_{RG} and its polynomial fitting are illustrated in

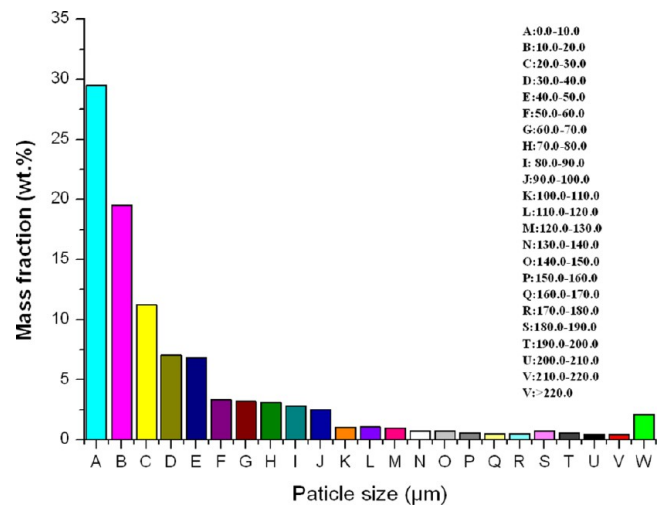


Figure 7. Particle size distribution of the ZD coal.

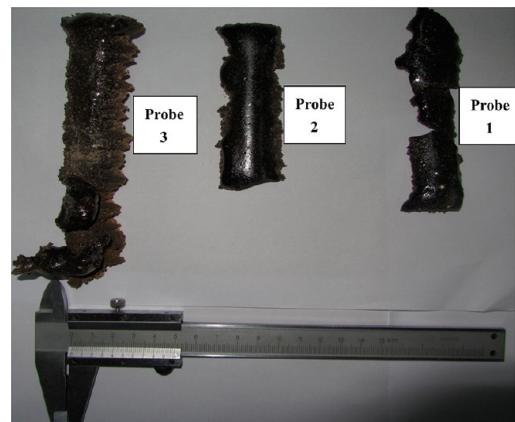


Figure 8. Photo of ash deposits from different deposition probes.

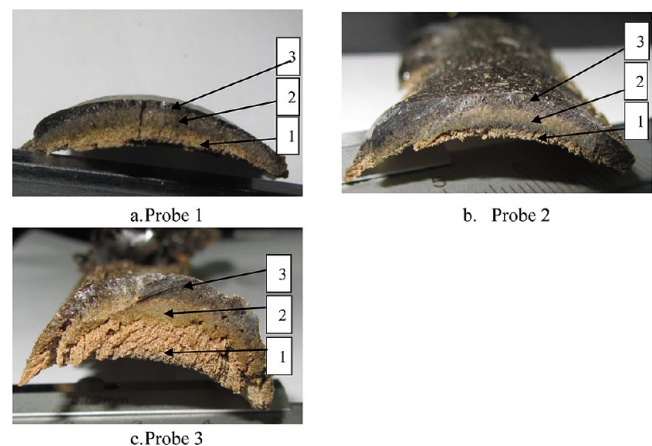


Figure 9. Cross sections of slags collected on different probes.

Figure 5. The corresponding relationship between T and X_{RG} can be expressed by a polynomial function, as in eq 9.

$$T = -1313.49055 + 6403.77022X_{RG} - 4792.10272X_{RG}^2 + 1099.71623X_{RG}^3 \quad (9)$$

Table 3 gives the setting temperatures and the corresponding calculated values according to eq 9. The errors are also given in Table 3. Apparently, the errors of the temperature are within -17.08 to 10.14 °C,

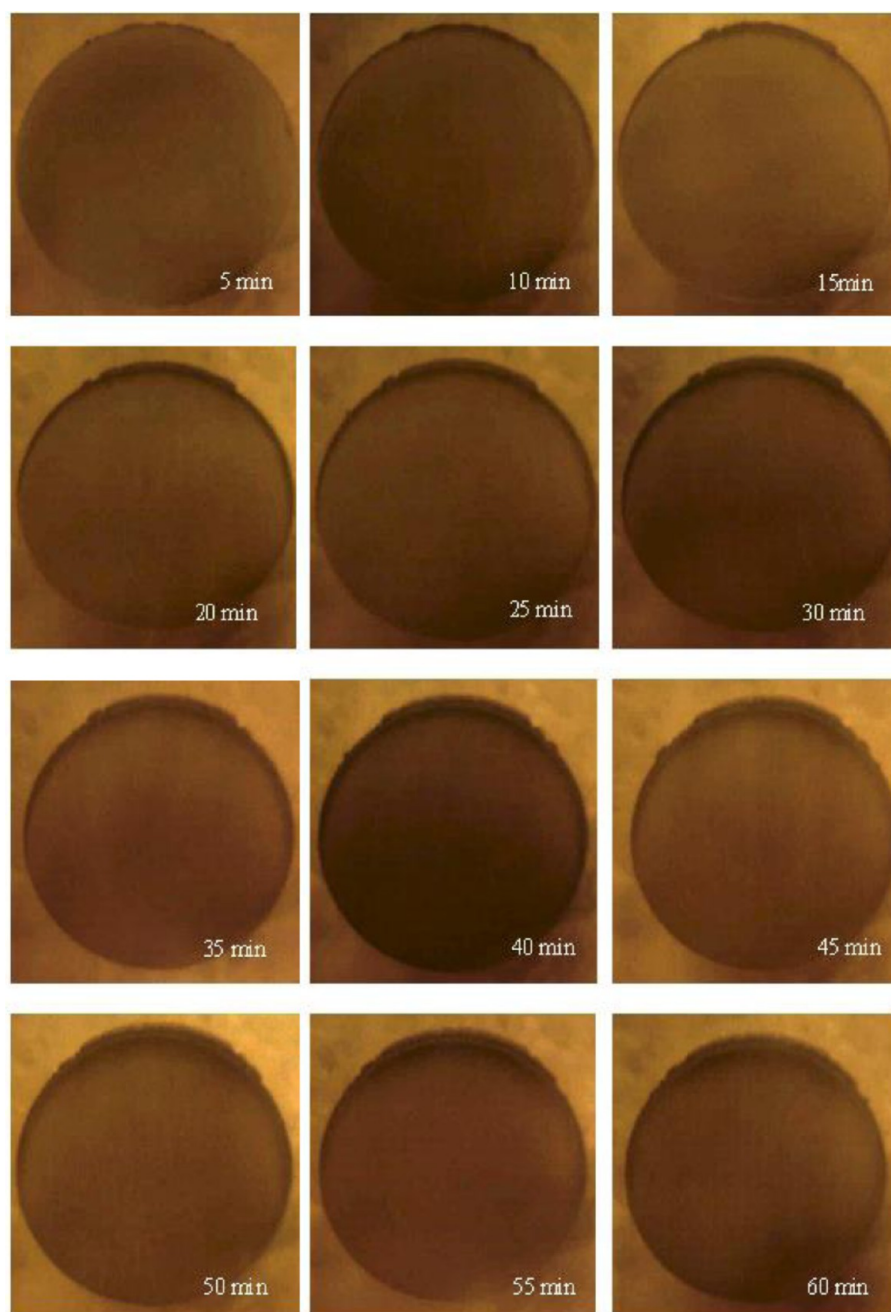


Figure 10. Photos of ash deposit in initial 60 min produced by CCD.

which are far less than the actual temperatures. Consequently, it can be concluded that this technique is available for the pilot scale applications.

2.6. Fuels. ZD coal was applied to feed in the pilot scale furnace during the experiment. Table 4 shows the proximate and ultimate analysis, gross heating value, ash melting temperature, and chemical compositions of the ZD coal. Obviously, the ash is rich in sodium-oxide with 8.31 wt % of the total sum. During the experiment, a low-temperature oxygen-plasma ashing instrument has been used to produce ash according to Standards Australia 2000. Then, the produced low-temperature ash (LTA) is analyzed by XRD. At last, the Rietveld-based technique is applied to quantify the relative proportions of crystalline phase in the LTA.^{9,21–23} The XRD pattern of the LTA is illustrated in Figure 6 and Table 5 shows the corresponding mineral composition of the LTA. Obviously, it can be observed that quartz, calcite, and halite are the dominant mineral phases of the LTA. Additionally, hematite is present in significant proportion in the LTA sample. Anhydrite is also found in the sample with a less amount. According to Ward et al., this

mineral phase is formed by artifacts of the plasma ashing process.²² Additionally, the coal is milled before experiment. A Malvern particle size analyzer is applied to measure the particle size distribution of the pulverized coal. The corresponding analysis result is illustrated in Figure 7.

2.7. Analytical Methods. The layer structures of the slagging deposits are separated and the samples are powdered until the average particle size was less than 74 μm . Subsequently, a PANalytical X'Pert PRO diffractometer system using Cu K α radiation is used to analyze the mineralogy of the samples. Scans were run from 5° to 80° 2 θ . The increment of a step is 0.0167°, and the corresponding counting time of a step is 130 s. In addition, the acceleration voltage is 40 kV and the corresponding current is 40 mA. The quantitative mineral compositions of the ash deposits were obtained by using Rietveld-based method.²⁴ Meanwhile, other portions of the slagging deposits were embedded into epoxy resin. The deposits mounted in resin were cut, grinded, and polished to get a smooth cross-section. The cross sections were coated

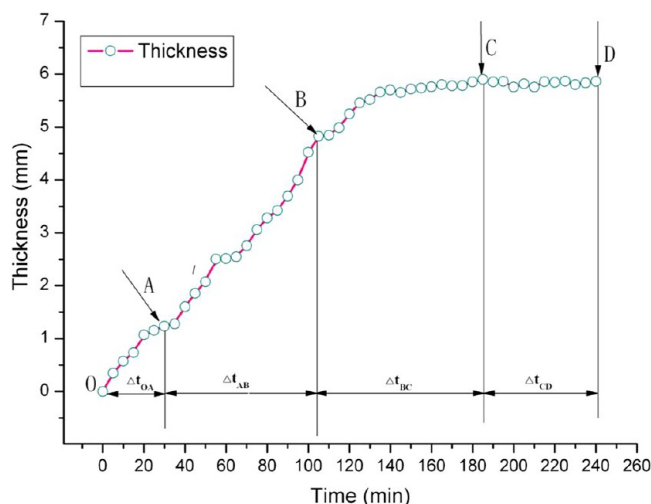


Figure 11. Change of deposit thickness versus time on the second probe.

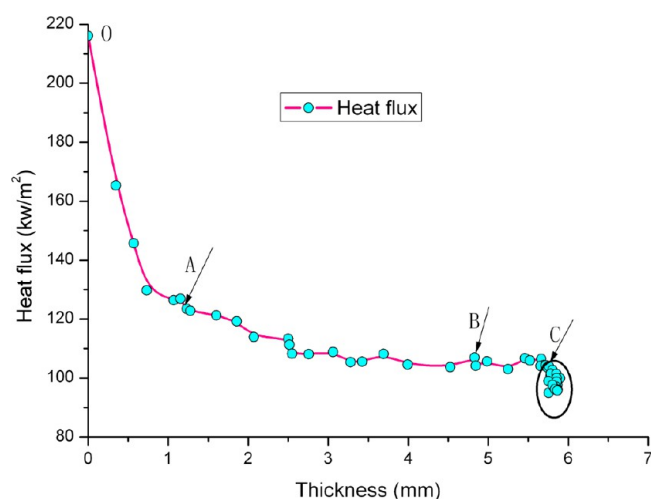


Figure 12. Variation of heat flux through the second probe with deposit growth.

with gold and analyzed by Sirion 100 thermal field scanning electron microscopy (FSEM) to obtain the microstructure of the deposits. Meanwhile, the chemical composition of the deposits are determined by GENESIS 4000 energy dispersive X-ray spectroscopy (EDX) equipped on FSEM.

3. RESULTS AND DISCUSSION

3.1. Visual Inspection of the Deposits. The exposure time of the deposition probes in the furnace is 4 h. Figure 8 illustrates the collected slagging deposits. The three ash deposits located from left to right correspond to probe 3, probe 2, and probe 1, respectively. Apparently, the color depth of the deposit surface for probe 3 is lighter than those of other deposits, as illustrated in

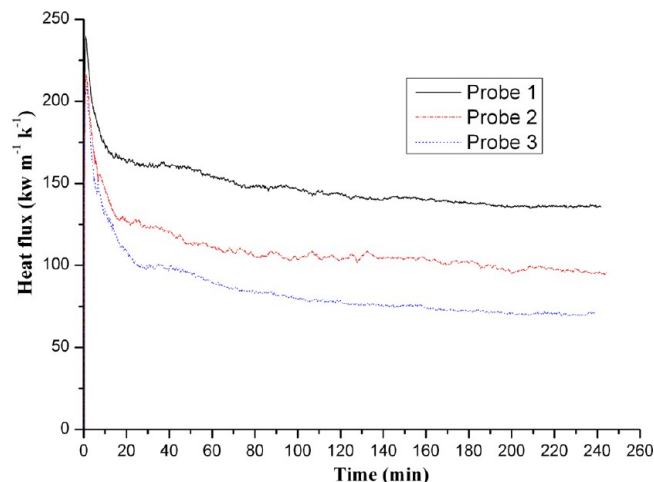


Figure 13. Heat flux through the three probes as function of time.

Figure 8. It may be because the temperature where probe 3 locates is lower than those where the other two probes locate, which may result in less sintering degree of deposit on probe 3 than those on the other two probes.

Figure 9 shows the cross sections of the three deposits. Due to the different colors and hardness, all the three deposits present a clear layered structure. Along deposit thickness direction (from inner to outer), the deposit on probe 1 includes three layers (i.e., layer 1 (the initial layer), layer 2 (the sintered layer), layer 3 (the slag layer)).¹⁰ The other two deposits collected on probe 2 and probe 3 also appeared the same phenomenon. Niu et al. and Zhang et al. found analogous phenomena for ash deposits of other fuels.^{25,26} The sintered layer corresponds to the early stage of sintering. It mainly involves densification and shrinkage of ash particles. The slag layer corresponds to the later stage of sintering. It principally refers to the appearance of melt. The stable stage means that the deposit thickness fluctuates in a narrow range and regresses to a constant value. Apparently, the initial layer appears no significant sintering with porous and unconsolidated particles. The sintered layer and slag layer present seriously sintered with dense structure. Moreover, due to the different sintering degree of the three layers of deposits, the color depth of the three layers increases with the deposit growth direction, as illustrated in Figure 9. In addition, the thickness of the deposit on probe 3 is significant larger than those of the other two deposits. The deposit thickness for probe 1 is equivalent to that for probe 2.

3.2. Deposit Growth on Probe 2. In the experiment, there will be too many deposit images produced by the CCD camera because the frame rate of the camera is set as 3 Frame/second. In consequence, the deposit thickness is determined by the digital image technique, which extracts deposit images from the recorded video. The corresponding frequency is one image per 5 min. Figure 10 shows the method of image extraction from the recorded video in this study.

Table 6. Parameters of Deposit Growth on the Second Probe

| case | stage of growth | time Δt (min) | thickness augementer (mm) | slope (mm/min) | ratio of heat flux decrement vs thickness augementer ($ \Delta q /\Delta h$, kw/(m ² ·mm)) | stable thickness (mm) | stable heat flux (kw/m ²) |
|---------|-----------------|-----------------------|---------------------------|----------------|---|-----------------------|---------------------------------------|
| ZD coal | stage 1 | 30 | 1.23 | 0.041 | 75.23 | 5.85–5.89 | 98.8 |
| | stage 2 | 75 | 3.60 | 0.048 | 4.58 | | |
| | stage 3 | 80 | 1.07 | 0.0134 | 7.96 | | |
| | stage 4 | >55 | 0 | 0 | 0 | | |

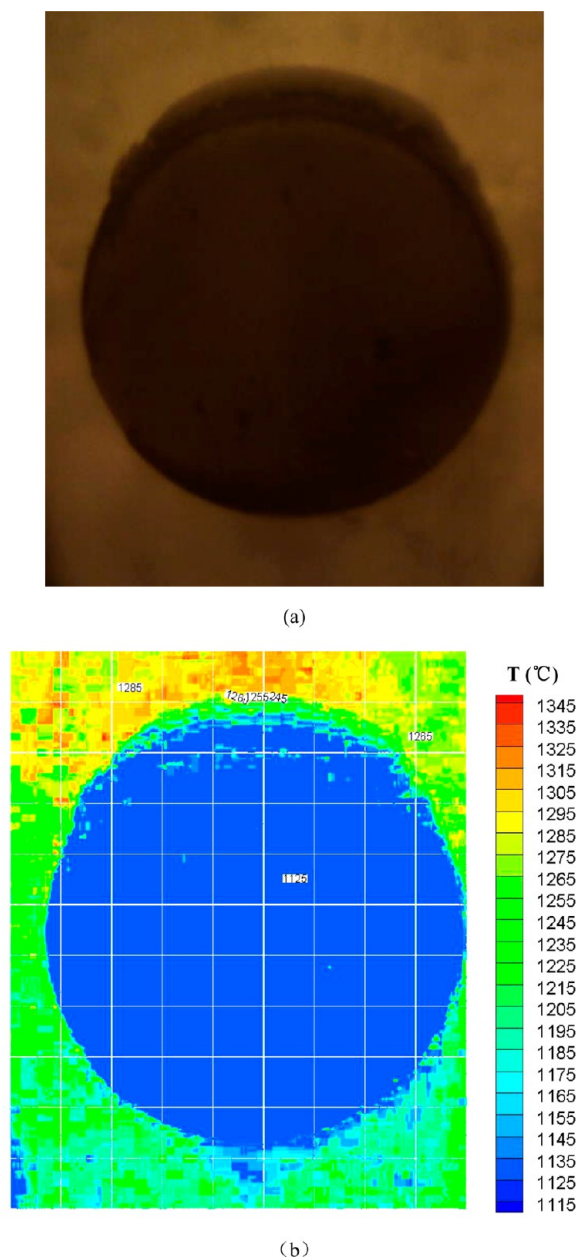


Figure 14. Typical deposit image and corresponding distribution of the deposit surface temperature.

Figure 11 shows the change of deposit thickness versus time on probe 2. Additionally, the corresponding change of heat flux through the probe with deposit growth is illustrated in Figure 12. According to different slopes, the curve in Figure 11 can be separated into four segments. In consequence, this result reveals that the deposit growth process is mainly composed of four stages (i.e., stage 1, stage 2, stage 3, and stage 4). This result is in accordance with the observation mentioned in chapter 3.1 that all the three ash deposits have three layered structures. Apparently, the deposit growth achieves stable stage, its corresponding thickness fluctuates in a narrow range and regresses to a fixed value, as shown in Figure 11. This may be because that the force acting on the deposit surface can be balance by surface force, gravity, and viscosity when its surface was molten.

Table 6 shows the various parameters of the ash deposit growth for probe 2. The deposit growth rates of the four stages are 0.041, 0.048, 0.0134, and 0 mm/min, corresponding to stages

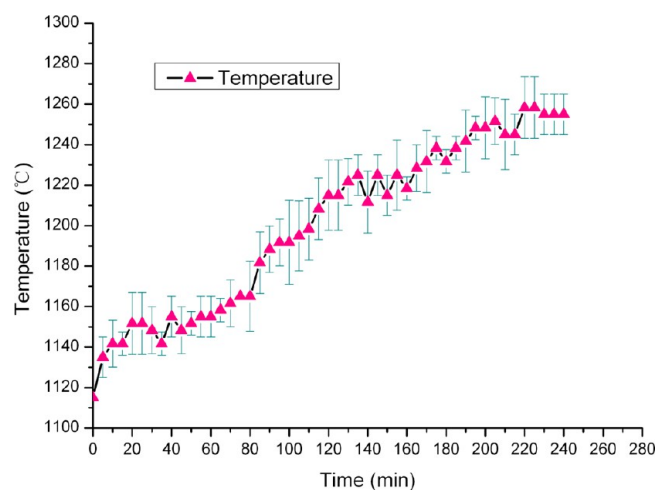


Figure 15. Variation of the deposit surface temperature with time on probe 2.

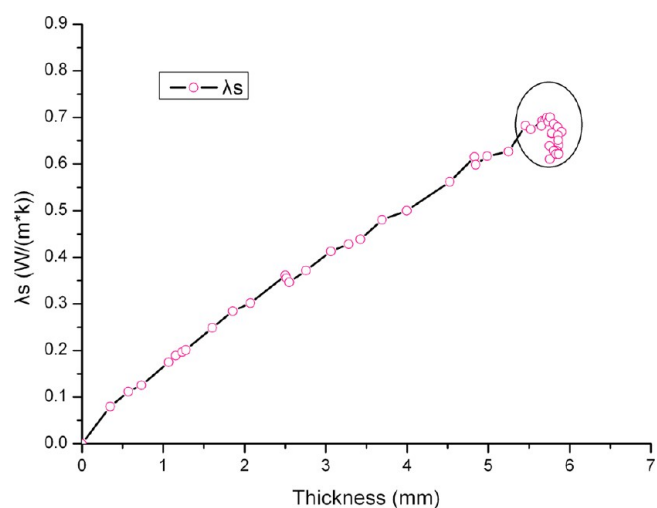


Figure 16. Variation of average effective heat conductivity of the deposit with deposit growth.

1, 2, 3, and 4, respectively. Obviously, the rates in stage 3 is evidently smaller than those in stages 1 and 2, as illustrated Figure 11. In addition, the duration time of the first three stages are 30, 75, and 80 min, respectively.

An interesting observation can be made that the heat flux decreases dramatically at initial stage, as shown in Figure 12. The corresponding ratio of decrement of heat flux to augments of thickness is up to $75.23 \text{ kW m}^{-2} \text{ mm}^{-1}$, as given in Table 6. This result suggests that the initial layer of deposit has a relatively low thermal conductivity. This may be a reason that the structure of initial layer is very porous and involves no evident melt, as described in section 3.1. However, the heat flux presents a moderate decline with ash deposit growth for stages 2 and 3, as illustrated in Figure 12. For stages 2 and 3, the corresponding ratios of heat flux decrement to thickness augments are 4.58, $7.96 \text{ kW m}^{-2} \text{ mm}^{-1}$, respectively. Obviously, the two values are evidently less than that for the initial stage. This may be caused by more serious sintering degree and molten fraction in the later two stages than that in the initial stage, with more molten fraction in stage 2 and stage 3. Meanwhile, an interesting observation can be made that there are a few data symbols aggregating in an ellipse, as shown in Figure 12. This may result from a little change for the

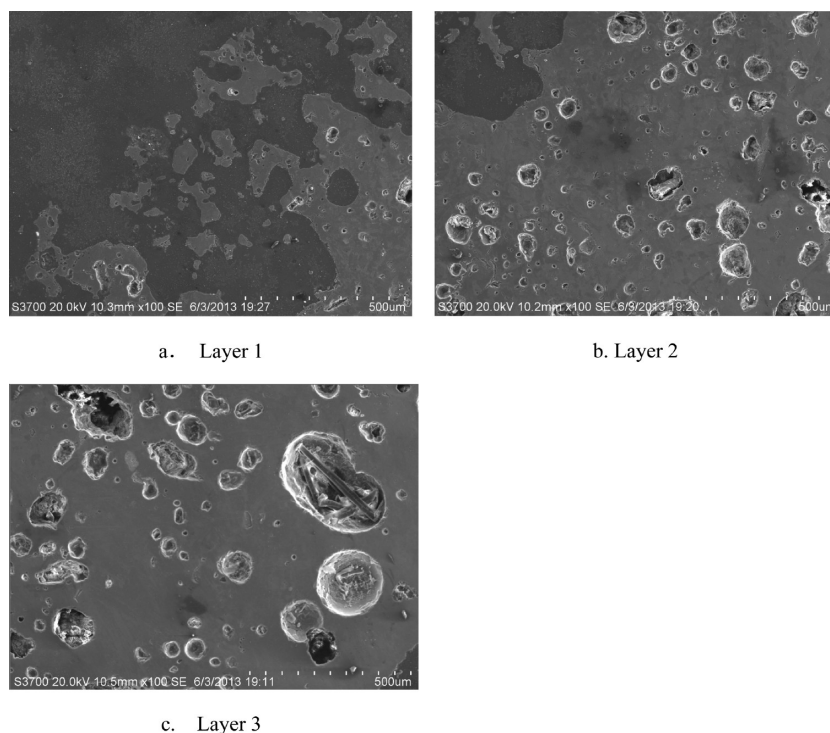


Figure 17. SEM photos of cross-section of each layer of the deposit on probe 1.

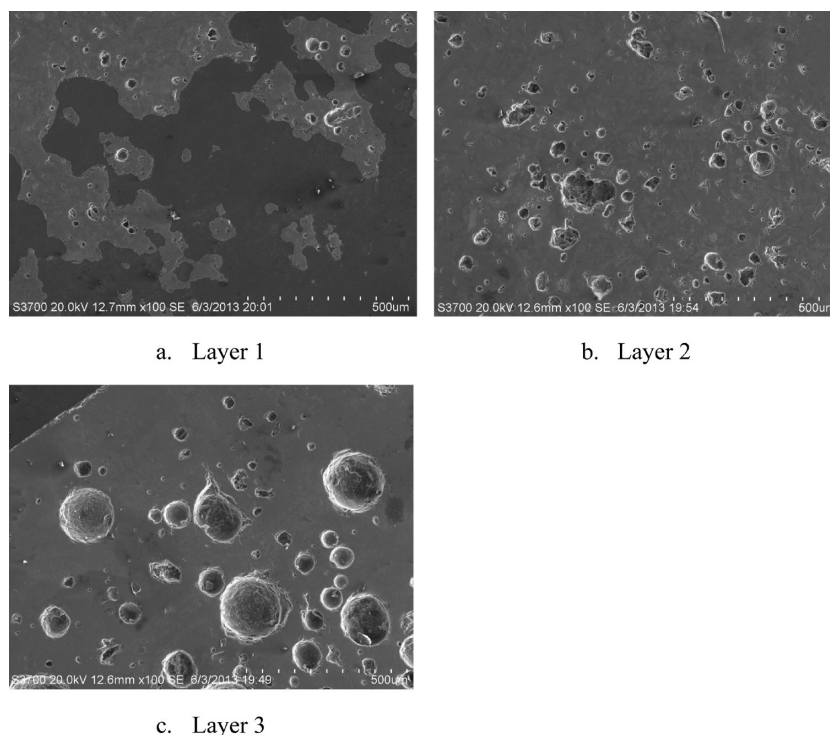


Figure 18. SEM photos of cross-section of each layer of the deposit on probe 2.

deposit thickness and the corresponding heat flux at stage 4. Meanwhile, the pore structures are continuously produced and ruptured into the ash deposit at this stage.

3.3. Heat Transfer Characteristics for the Three Probes.

Figure 13 illustrated the variation of heat flux through the three probes with time. The three curves in this figure show the same trend. Once the deposit probe is inserted into the furnace, the heat flux can achieve the maximum value in seconds. Then,

the heat flux declines with deposit growth, and at last, the heat flux value fluctuates in a narrow range. The corresponding stable heat fluxes through the three deposit probes are 135.50, 95.72, and 71.26 kw m^{-2} , respectively. As shown in Figure 9, the deposit thickness for probe 1 is equivalent to that for probe 2. Moreover, the two deposits have similar sintering degree and chemical composition which was verified by the XRD analysis in section 3.6. Consequently, the higher temperature where probe 1 located

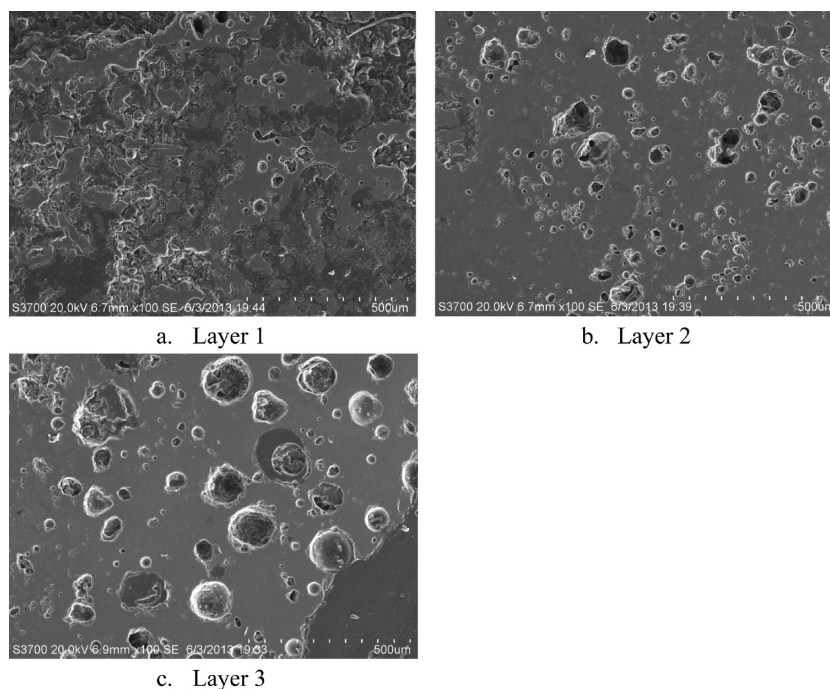


Figure 19. SEM photos of cross-section of each layer of the deposit on probe 3.

Table 7. Chemical Compositions of Ash Deposits Collected on Different Probes Identified by SEM-EDX

| sample | | K ₂ O | CaO | TiO ₂ | SiO ₂ | Na ₂ O | MgO | Al ₂ O ₃ | Fe ₂ O ₃ |
|---------|---------|------------------|-------|------------------|------------------|-------------------|------|--------------------------------|--------------------------------|
| probe 1 | layer 1 | 0.27 | 23.68 | 0.88 | 44.59 | 5.59 | 2.77 | 15.62 | 3.28 |
| | layer 2 | 0.21 | 21.21 | 1.17 | 46.37 | 3.34 | 2.33 | 15.94 | 3.78 |
| | layer 3 | 0.17 | 29.71 | 0.65 | 39.12 | 3.31 | 3.75 | 14.77 | 5.12 |
| probe 2 | layer 1 | 0.22 | 30.58 | 0.80 | 43.74 | 3.55 | 3.16 | 11.87 | 3.17 |
| | layer 2 | 0.21 | 19.11 | 1.78 | 45.36 | 3.13 | 1.23 | 19.92 | 5.83 |
| | layer 3 | 0.20 | 28.66 | 1.07 | 38.93 | 2.80 | 3.02 | 15.05 | 7.04 |
| probe 3 | layer 1 | 0.23 | 32.59 | 1.59 | 32.81 | 2.84 | 4.66 | 16.44 | 6.42 |
| | layer 2 | 0.21 | 31.64 | 0.83 | 45.11 | 2.68 | 2.43 | 10.54 | 3.96 |
| | layer 3 | 0.19 | 29.79 | 1.32 | 39.66 | 2.50 | 2.95 | 15.33 | 5.50 |

may result in significantly larger heat flux through probe 1 than probe 2. Meanwhile, the heat flux through probe 3 is the lowest between the three probes. This may be caused by the lower heat conductivity of deposit, larger deposit thickness (see Figure 9), and lower temperature where probe 3 locates.

3.4. Measurement of Surface Temperature and Average Effective Thermal Conductivity for the Deposit on Probe 2. During the experiment, the color deposit images were applied to calculate the deposit surface temperature by using the image processing system. It was similar to the procedure of the deposit thickness calculation, one deposit image per five minutes was calculated by the system. Figure 14a illustrates a typical deposit image in the stable stage of the ash deposit growth. The corresponding distribution of deposit surface temperature is presented in Figure 14b.

The change of the deposit surface temperature versus time on probe 2 is shown in Figure 15. An interesting observation can be made that the deposit surface temperature increases gradually during the deposit growth and then fluctuates around a certain value — 1255 °C. It may be a result of heat transfer deterioration with increasing deposit thickness. When the deposit surface temperature increased to ash flow temperature (FT), the deposit surface was melted and the deposit thickness did not increase any more. According to Table 3, the FT of the ZD coal ash was 1231 °C measured in weak reducing atmosphere. In con-

sequence, the ash melting point is slightly more than 1231 °C in actual pilot scale furnace.

To fully understand the deposit growth characteristic, the deposit thickness and the corresponding surface temperature are combined to determine the average effective heat conductivity of ash deposit. The ash particles mainly deposit on the upstream side of the probe when the deposition probe is inserted into the furnace. During the deposit formation, the deposit is generally similar to a half-ellipse in shape, as shown in Figure 2b. Consequently, the heat transfer through the probe can be determined by the mathematical model of cylindrical wall heat conduction. To simplify the calculation, the heat transfer is assumed one dimension and direction of heat flux, which penetrates through point A to B in Figure 2b. Therefore, the heat flux through the probe can be determined with eq 10:

$$q = \frac{\lambda(t_2 - t_1)}{r \ln\left(\frac{r_2}{r_1}\right)} \quad (10)$$

where λ represents the thermal conductivity of deposition probe material; r represents the radius of deposition probe; r_1 represents the distance from point B to the center of the probe in Figure 2b; r_2 represents the distance from point A to the center of the probe in Figure 2b; t_2 and t_1 are outer and inner surface temperatures of deposit probe, respectively.

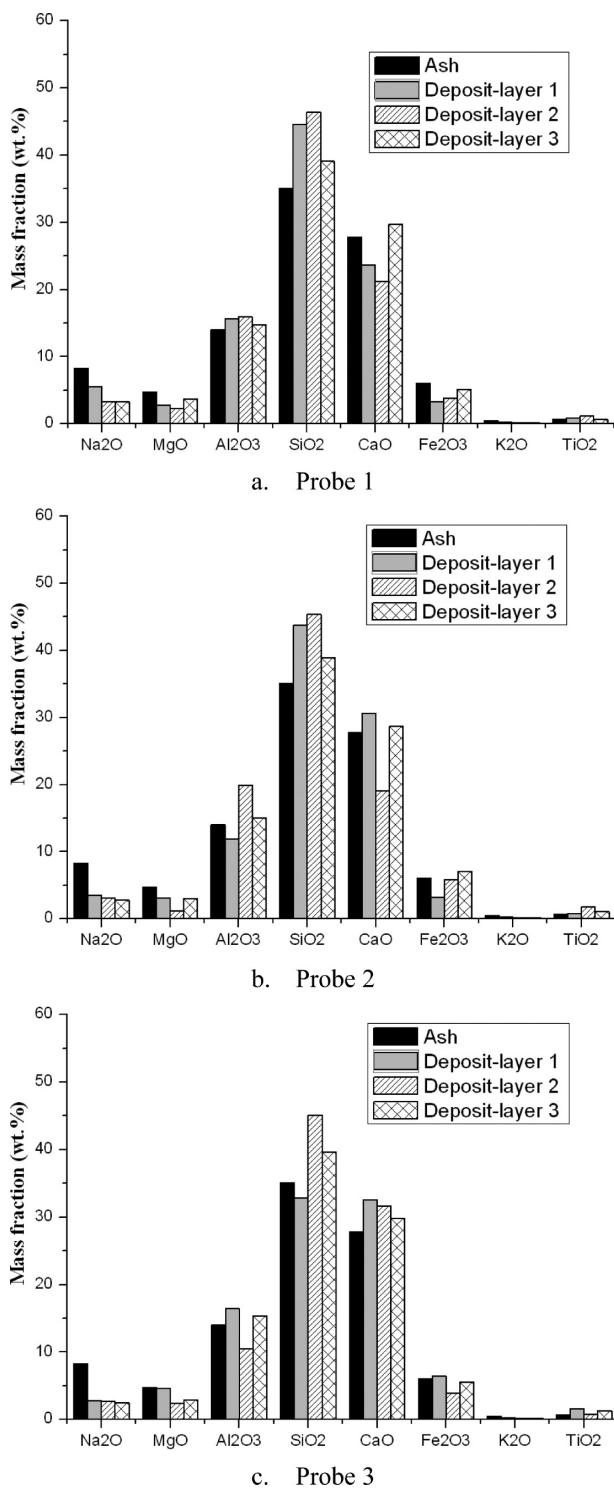


Figure 20. Comparison of the composition of ash with those of deposits.

According to Fourier's law, the balance between conductive heat flux through the different layers of the deposit and conductive heat flux through the ash deposition probe yields eq 11,

$$q = \frac{\lambda(t_2 - t_1)}{r \ln\left(\frac{r_2}{r_1}\right)} = \frac{\bar{\lambda}_s(t_s - t_2)}{\delta} \quad (11)$$

where $\bar{\lambda}_s$ is the average effective heat conductivity of the deposit; δ is the deposit thickness; t_s is the average deposit surface temperature.

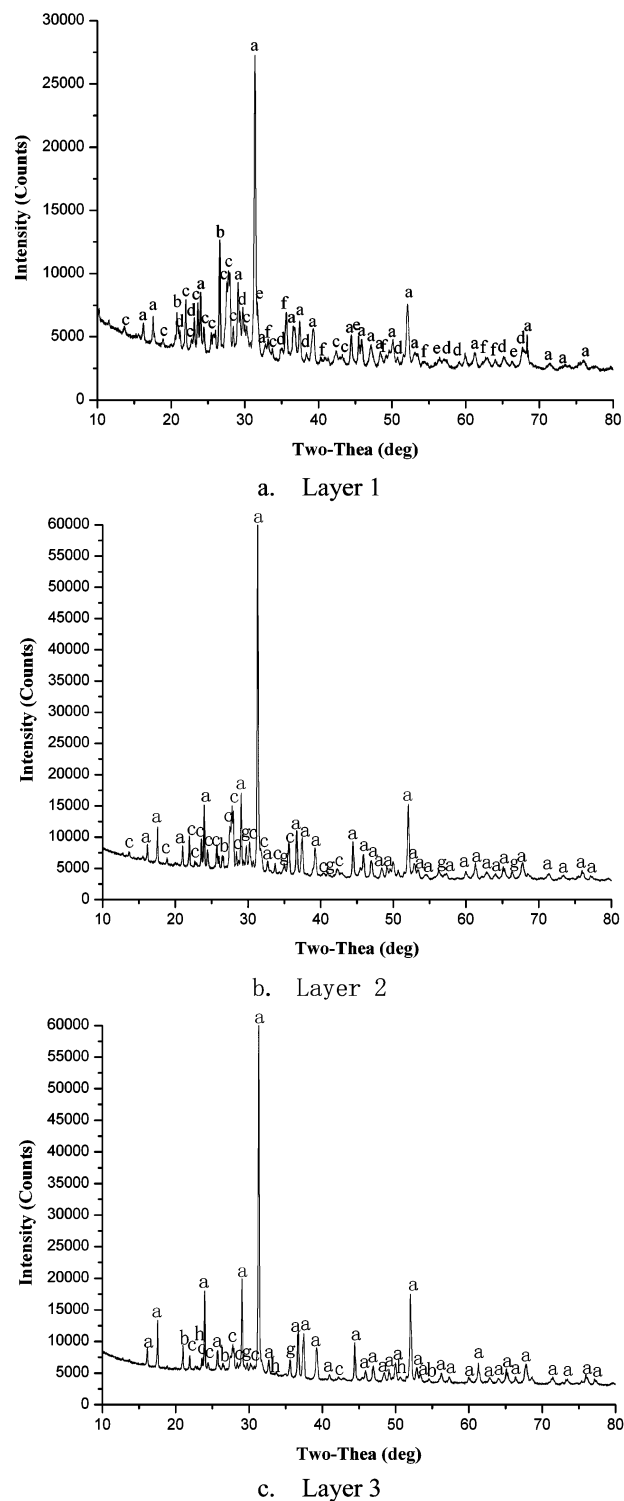


Figure 21. XRD pattern of the ash deposit on probe 1. (a) Gehlenite- $\text{Ca}_2(\text{Al}(\text{AlSi})\text{O}_7)$; (b) quartz-SiO₂; (c) anorthite- $\text{CaAl}_2\text{Si}_2\text{O}_8$; (d) nepheline- $\text{KNa}_3(\text{AlSiO}_4)_4$; (e) halite-NaCl; (f) hematite-Fe₂O₃; (g) diopside- $\text{CaMg}(\text{SiO}_3)_2$; (h) mullite- $\text{Al}_6\text{Si}_2\text{O}_{13}$.

After the heat flux through the deposit probe was calculated by using eq 10, the average effective thermal conductivity of deposit can be obtained by

$$\bar{\lambda}_s = \frac{q\delta}{(t_s - t_2)} \quad (12)$$

Table 8. Mineralogy of Ash Deposit on Probe 1 (wt %)

| phase | layer 1 | layer 2 | layer 3 |
|---|---------|---------|---------|
| glass | 56.7 | 41.2 | 30.6 |
| gehlenite- $\text{Ca}_2(\text{AlSi})\text{O}_7$ | 17.6 | 28.8 | 46.1 |
| quartz- SiO_2 | 2.8 | 0.5 | 1.1 |
| aaorthite- $\text{CaAl}_2\text{Si}_2\text{O}_8$ | 14.4 | 23.9 | 17.8 |
| nepheline- $\text{KNa}_3(\text{AlSiO}_4)_4$ | 6.3 | | |
| halite- NaCl | 1.4 | | |
| hematite- Fe_2O_3 | 0.8 | | |
| diopside- $\text{CaMg}(\text{SiO}_3)_2$ | | 5.6 | 3.5 |
| mullite- $\text{Al}_6\text{Si}_2\text{O}_8$ | | | 1.0 |

Figure 16 illustrates the variation of average effective thermal conductivity of the deposit versus deposit thickness. It can be found that the average effective thermal conductivity of the deposit increases linearly with deposit growth. This results from the increasing sintered degree with deposit growth. Sintering evidently changed the microstructure of ash deposit, which resulted in the densification of deposit. Meanwhile, sintering also altered the mineralogy of the deposit, which is proved by the XRD results. During the deposit formation of initial layer, the average thermal conductivity of deposit increased a factor of 2.45 from $0.07987 \text{ W m}^{-1} \text{ K}^{-1}$ to $0.19625 \text{ W m}^{-1} \text{ K}^{-1}$, as illustrated in Figure 16. This value approached the heat conductivity of air at a specific deposition temperature. This may because the very porous deposit in initial layer is composed of incompact particles, which is verified by microstructure of ash deposit in section 3.5. At the stable stage of deposit growth, the average effective thermal conductivity increased to $0.70041 \text{ W m}^{-1} \text{ K}^{-1}$ and fluctuated at this value. Consequently, some data symbols with 5.8 mm deposit thickness aggregate in an ellipse, as shown in Figure 15. This may be a result of continuous development and rupture of bubble structure in deposit by sintering.

3.5. Microstructure of the Ash Deposits. Figures 17–19 illustrate representative SEM images captured from cross-sectioned ash deposits from the three probes. It can be found that the three deposits have similar microstructure. Figure 17 presents the cross-sectional structures of the three layers of the deposit on probe 1. It is clear that the three layers have significantly different microstructures due to different sintering degree. The initial layer (layer 1) appears loose structure with no evident agglomerates and bridges formation, ash shown in Figure 16a. Meanwhile, void space between deposit area is filled by the epoxy resin. This microstructure will cause heat conductivity of layer 1 to be relatively low, which is in accordance with the reports described in section 3.2. As illustrated in Figure 17b, the sintered layer (layer 2) includes many irregular pores with small diameters. In addition, the sintered layer area presents a continuous phase, which is caused by serious sintering. In addition, many huge pores with diameters bigger than $200 \mu\text{m}$ (see Figure 17c) are presented in the slag layer. It results from the further shrinkage and melting of ash particles by the high temperature. As shown in Figures 18 and 19, similar microstructures shown in Figure 17 can be observed from the SEM photos of cross-sectional structures. The initial layer presents no significant melting and the void space filled by the epoxy resin, as shown in Figure 18a and Figure 19a. The sintered layer and the slag layer appear significant sintering with more compact morphology than the initial layer (see Figure 18b, c and Figure 19b, c). This results in high heat conductivities of the sintered layer and slag layer, which are consistent with the result that the average heat conductivity of ash

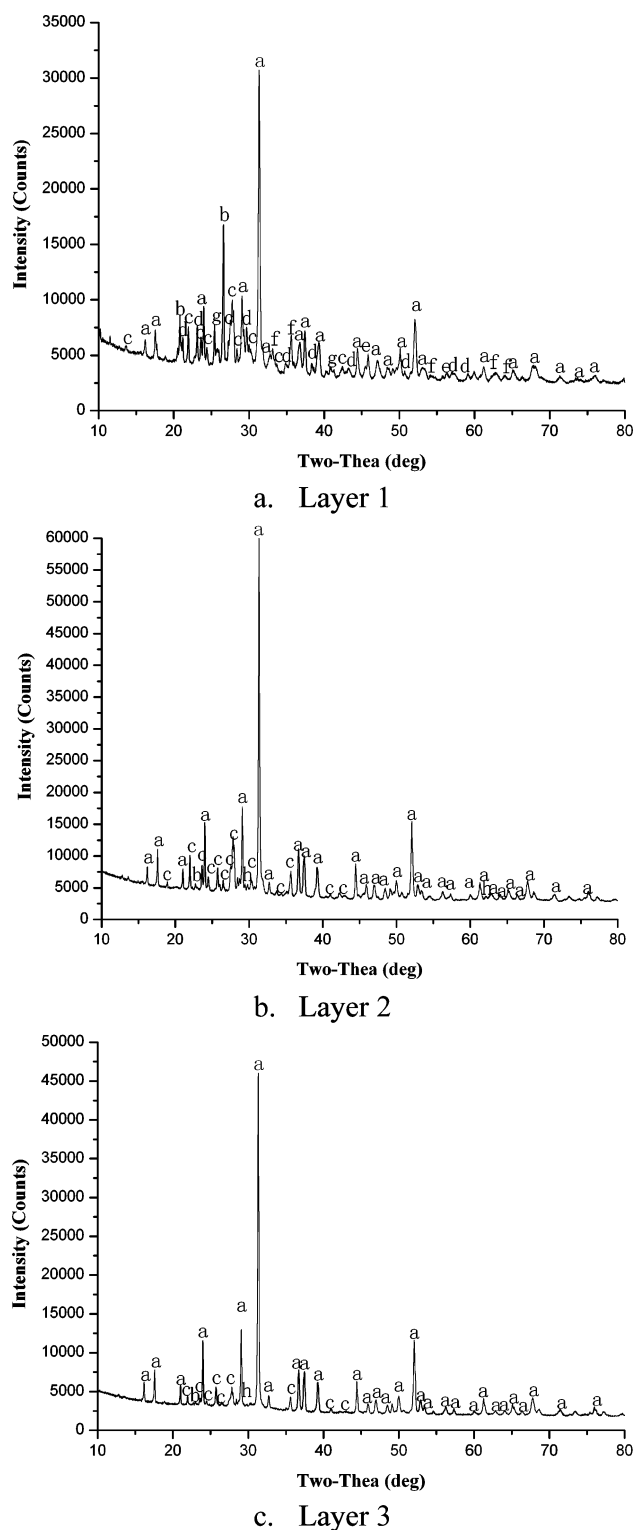


Figure 22. XRD pattern of the ash deposit on probe 2. (a) Gehlenite- $\text{Ca}_2\text{Al}(\text{AlSi})\text{O}_7$; (b) quartz- SiO_2 ; (c) anorthite- $\text{CaAl}_2\text{Si}_2\text{O}_8$; (d) nepheline- $\text{KNa}_3(\text{AlSiO}_4)_4$; (e) halite- NaCl ; (f) hematite- Fe_2O_3 ; (g) anhydrite- CaSO_4 ; (h) diopside- $\text{CaMgSi}_2\text{O}_6$.

deposit on probe 2 increase with deposit growth, as illustrated in Figure 15.

3.6. Chemical Composition and Mineralogy of the Deposits. The analysis results from the SEM-EDX were normalized to 100% and presented in Table 7 in oxides form. The corresponding results reveal that the main elements of the

Table 9. Mineralogy of Ash Deposit on Probe 2 (wt %)

| phase | layer 1 | layer 2 | layer 3 |
|--|---------|---------|---------|
| glass | 54.2 | 43.3 | 34.6 |
| gehlenite- $\text{Ca}_2(\text{Al}(\text{AlSi})\text{O}_7)$ | 19.9 | 33.7 | 50.2 |
| quartz- SiO_2 | 4.0 | 0.7 | 1.0 |
| anorthite- $\text{CaAl}_2\text{Si}_2\text{O}_8$ | 11.7 | 20.1 | 12.6 |
| nepheline- $\text{KNa}_3(\text{AlSiO}_4)_4$ | 6.6 | | |
| halite- NaCl | 1.0 | | |
| hematite- Fe_2O_3 | 1.5 | | |
| diopside- $\text{CaMg}(\text{SiO}_3)_2$ | | 2.2 | 1.6 |
| anhydrite- CaSO_4 | 1.1 | | |

ash deposits are Ca, Si, Al, Fe, Na, and Mg, while Ti and K are relatively low. For probe 1, the contents of K and Na decline with the deposit growth direction, while the concentrations of Fe, Mg, and Ca increase, as shown in Table 7. Moreover, the maximum concentrations of Al and Si are in layer 2. The bulk compositions of the coal ash and deposit have been compared, and the corresponding results are illustrated in Figure 20a. It is clear that the three layers of the deposit on probe 1 contain more SiO_2 and Al_2O_3 than ash, which suggests that these two elements play crucial role in deposit formation. Meanwhile, the concentrations of sodium-oxide in the three layers of the deposit are much lower than that in coal-ash. It may be because sodium species in the coal are generally mobile and enter the gas phase in terms of NaCl during the combustion process.²⁷ NaCl vapors adhere to the probe mainly through the homogeneous condensation in the flue gas with formation submicrometer particles or heterogeneous condensation on the incoming Si–Ca-bearing fly ash particles prior to reaching the surface of probe.²⁸ Subsequently, the condensed NaCl react with silicon to form sodium silicates or react with sulfur-containing compounds to form K_2SO_4 . However, the ZD coal is characterized by high level sodium in the coal ash, which accounts for 8.31 wt % of the ash species. But the concentration of chlorine is far lower in the coal-ash. In consequence, many sodium species end up with bottom deposits or fly ash particles. The further study of the mineral phase in the deposit on probe 1 is conducted by using XRD, and the results are illustrated in Figure 21. Gehlenite, anorthite, and nepheline are the main identified crystalline phases in the initial layer of the ash deposit on probe 1. In addition, for the sintered layer, the dominant mineral phases are gehlenite, anorthite, and diopside. Similarly, it can be found that the main components are also gehlenite, anorthite, and diopside for the slag layer. The quantitative mineral compositions of the slagging deposit are given in Table 8. In addition, the content of gehlenite in the slag increases with the deposit thickness, as given in Table 8. It suggests that the formation of gehlenite needs a high temperature condition.²⁹ Moreover, the content of amorphous phase decreased with the deposit growth.

For probe 2, it can also be observed that the contents of Na and K decline with the deposit growth direction, as given in Table 7. Nevertheless, the concentration of iron increases with the thickness direction of the deposit (from inner to outer). Additionally, the sintered layer has the maximum content of Si and Al. This may be a reason that an abundance of aluminosilicates are formed in the sintered layer, which is verified by the XRD results that the sintered layer contains two major crystalline phases: gehlenite and anorthite (see Figure 22b). The comparison of the bulk composition between the slag and ash is illustrated in Figure 20b. Obviously, it can be seen that the sintered layer and slag layer contain more SiO_2 , Al_2O_3 , and

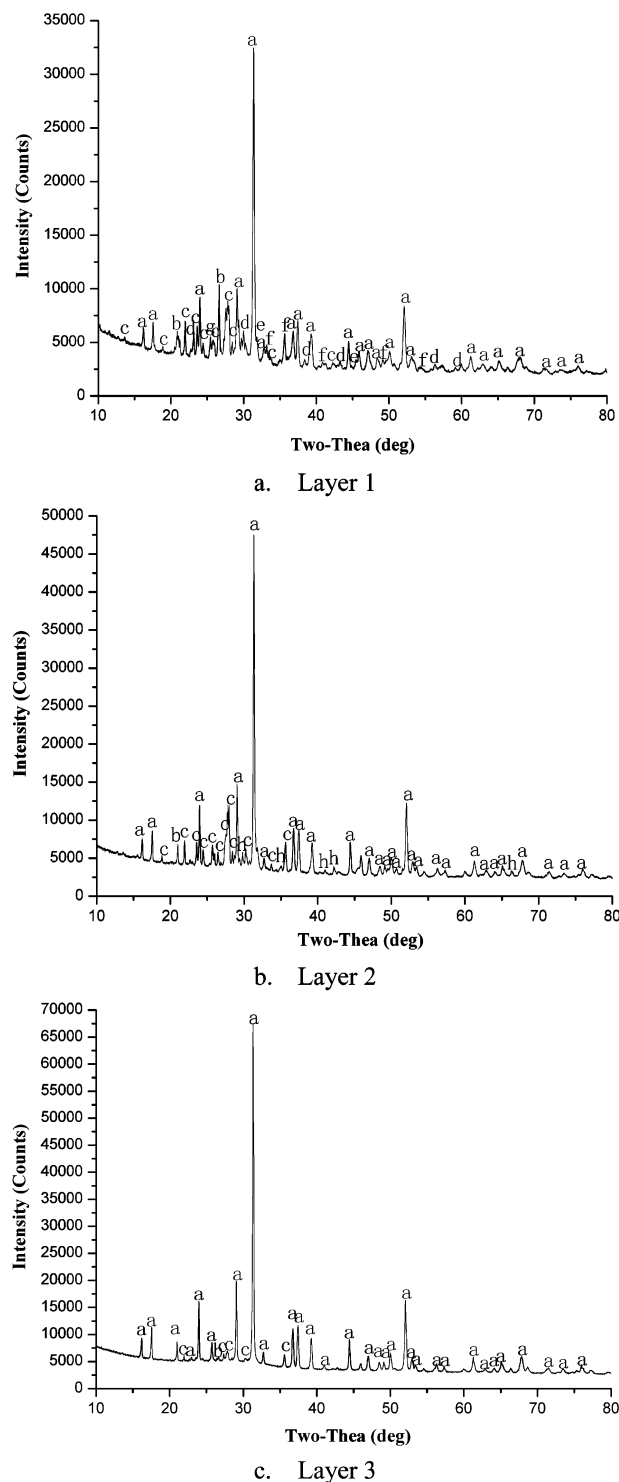


Figure 23. XRD pattern of the ash deposit on probe 3. (a) Gehlenite- $\text{Ca}_2\text{Al}(\text{AlSi})\text{O}_7$; (b) quartz- SiO_2 ; (c) anorthite- $\text{CaAl}_2\text{Si}_2\text{O}_8$; (d) nepheline- $\text{KNa}_3(\text{AlSiO}_4)_4$; (e) halite- NaCl ; (f) hematite- Fe_2O_3 ; (g) anhydrite- CaSO_4 ; (h) diopside- $\text{CaMgSi}_2\text{O}_6$.

Fe_2O_3 , which indicates that these elements play crucial role in formation of the sintered layer and slag layer. However, according to the XRD patterns shown in Figure 22, little Fe-bearing mineral phase is observed. This indicates that some low melting point eutectics have been produced by the reaction between iron oxide and aluminum silicates. And these eutectics cannot be identified by XRD. In addition, the XRD analysis

Table 10. Mineralogy of Ash Deposit on Probe 3 (wt %)

| phase | layer 1 | layer 2 | layer 3 |
|--|---------|---------|---------|
| glass | 57.8 | 46.3 | 32.5 |
| gehlenite- $\text{Ca}_2(\text{Al}(\text{AlSi})\text{O}_7)$ | 20.7 | 28.3 | 50.76 |
| quartz- SiO_2 | 1.8 | 1.1 | 1.8 |
| anorthite- $\text{CaAl}_2\text{Si}_2\text{O}_8$ | 14.5 | 21 | 12.9 |
| nepheline- $\text{KNa}_3(\text{AlSiO}_4)_4$ | 3.0 | | |
| halite- NaCl | 0.9 | | |
| hematite- Fe_2O_3 | 0.8 | | |
| diopside- $\text{CaMg}(\text{SiO}_3)_2$ | | 3.3 | 2.16 |
| anhydrite- CaSO_4 | 0.5 | | |

shown in Figure 22 indicates that gehlenite, anorthite, and nepheline are the dominant crystalline phases in the initial layer of the deposit. The major components of the sintered layer are gehlenite and anorthite, as presented in Figure 22b. Additionally, the slag layer has the similar mineral phase in comparison to the sintered layer, and the corresponding quantitative mineral compositions of the deposit were given in Table 9. It can be found that the concentration of gehlenite in the slag on probe 2 also increases along the deposit thickness direction. Moreover, the dominant components of the deposit on probe 2 are similar to those of slag on probe 1.

For probe 3, the concentrations of Na, K, and Ca decrease with the deposit growth, as given in Table 7. Other elements present no significant regular increment. The compositions of the coal ash and the deposit have been compared in this study, and the corresponding results are illustrated in Figure 20c. Obviously, it can be concluded that the contents of Al_2O_3 , SiO_2 , and Fe_2O_3 in the initial layer and the slag layer are more than those in ash. This suggests that these three elements will be of great importance to in the formation of the initial layer and slag layer with production of aluminum silicates. The mineralogy of the slag on probe 3 is also conducted by using XRD, as illustrated in Figure 23. Similar to the slags on probe 1 and probe 2, the main constituents of the initial layer of the slag on probe 3 are, gehlenite, and anorthite. In addition, the major compounds in the sintered layer of the slag are anorthite and gehlenite. The main crystalline phases identified in the slag layer were also gehlenite and anorthite. Additionally, Table 10 illustrates the mineral compositions of the ash deposits. Obviously, it can be found that the content of gehlenite increases along deposit thickness direction. This indicates that continuous formation of this crystalline phase at high temperatures.

4. CONCLUSIONS

A novel technique has been applied to measure the effective heat conductivity of ash deposits for ZD coal in pilot scale furnace. And the following conclusions can be drawn from the experimental results: (1) The growth process of the ash deposit on probe 2 is composed of four stages. This was in accordance with the layer structures of the ash deposits. The heat flux declined dramatically in the initial stage of ash deposit growth. It indicates that the thermal conductivity of the initial layer is lowest between the three layers. (2) The deposit surface temperature increased with time, and it finally fluctuated around 1255 °C. Meanwhile, the average effective heat conductivity of the ash deposit on probe 2 increased linearly with the deposit growth. (3) The XRD patterns of three deposits showed that these deposits had similar mineralogy in every layer structure. In addition, the contraction of gehlenite in the deposit increased with the deposit thickness direction (from inner to outer). The loss of amorphous phase is accompanied by a corresponding increase in mineral phase.

AUTHOR INFORMATION

Corresponding Author

*Tel: +86-571-87952598; Fax: +86-571-87951616. E-mail: zhouhao@cmee.zju.edu.cn.

Notes

The authors declare no competing financial interest.

ACKNOWLEDGMENTS

This work was supported by Zhejiang Provincial Natural Science Foundation of China (LZ12E06002), Key Technologies R&D Program of China (2011BAA04B01).

REFERENCES

- (1) Hare, N.; Rasul, M. G.; Moazzem, S. A Review on Boiler Deposition/Fouling Prevention and Removal Techniques for Power Plant. *Proceedings of the 5th IASME/WSEAS International Conference on Energy and Environment*, Cambridge, U.K., Feb 23–25; 2010.
- (2) Vamvuka, D.; Mistakidou, E.; Drakonaki, S.; Foscolos, A.; Kavouridis, K. Ash Quality of a Beneficiated Lignite from Ptolemais Basin, Northern Greece. *Energy Fuels* **2001**, *15*, 1181–1185.
- (3) Richards, G. H.; Slater, P. N.; Harb, J. N. Simulation of Ash Deposit Growth in pulverized Coal-Fired Pilot Scale Reactor. *Energy Fuels* **1993**, *7*, 774–781.
- (4) Arvelakis, S.; Folkedahl, B.; Johansen, K. D.; Hurley, J. Studying the Melting Behavior of Coal, Biomass, and Coal/Biomass Ash Using Viscosity and Heated Stage XRD Data. *Energy Fuels* **2006**, *20*, 1329–1340.
- (5) Kostakis, G. Mineralogical Composition of Boiler Fouling and Slagging Deposits and Their Relation to Fly Ashes: The Case of Kardias Power Plant. *J. Hazard. Mater.* **2011**, *185*, 1012–1018.
- (6) Wang, H.; Harb, J. N. Modeling of Ash Deposition in Large-Scale Combustion Facilities Burning Pulverized Coal. *Prog. Energy Combust. Sci.* **1997**, *23*, 267–282.
- (7) Ma, Z.; Iman, F.; Lu, P.; Sears, R.; Kong, L.; Rokanuzzaman, A. S.; McCollor, D. P.; Benson, S. A. A Comprehensive Slagging and Fouling Prediction Tool for Coal-Fired Boilers and Its Validation/Application. *Fuel Process. Technol.* **2007**, *88*, 1035–1043.
- (8) Naruse, I.; Kamihashira, D.; Khairil; Miyauchi, Y.; Kato, Y.; Yamashita, T.; Tominaga, H. Fundamental Ash Deposition Characteristics in Pulverized Coal Reaction under High Temperature Conditions. *Fuel* **2005**, *84*, 405–410.
- (9) Creelman, R. A.; Ward, C. R.; Schumacher, G.; Juniper, L. Relation between Coal Mineral Matter and Deposit Mineralogy in Pulverized Fuel Furnace. *Energy Fuels* **2013**, *27*, 5714–5724.
- (10) Tomeczek, J.; Wacławski, K. Two-Dimensional Modeling of Deposits Formation on Platen Superheaters in Pulverized Coal Boilers. *Fuel* **2009**, *88*, 1466–1471.
- (11) Wall, T. F.; Bhattacharya, S. P.; Zhang, D. K.; Gupta, R. P.; He, X. *Prog. Energy Combust. Sci.* **1993**, *19*, 487–504.
- (12) Allen, L. R.; Steven, G. B.; Larry, L. B. Experimental Measurements of the Thermal Conductivity of Ash Deposits: Part 1. Measurement Technique. *Energy Fuels* **2001**, *15*, 66–74.
- (13) Rezaei, H. R.; Gupta, R. P.; Bryant, G. W.; Hart, J. T.; Liu, G. S.; Bailey, C. W.; Wall, T. F.; et al. Thermal Conductivity of Coal Ash and Slags and Models Used. *Fuel* **2000**, *79*, 1697–1710.
- (14) Chikuma, H.; Kurimura, M.; Ichikawa, K.; Takahashi, T. Study on Growth Behavior and Heat Transfer of Ash Deposit. *Proceedings of the 3rd International Conference on Power Engineering*, Tokyo, Japan, July 13–17, 1997.
- (15) Huang, Y.; Yan, Y.; Riley, G. Vision-based measurement of temperature distribution in a 500-kW model furnace using the two-colour method. *Measurement* **2000**, *28*, 175–183.
- (16) Lu, G.; Yan, Y.; Colechin, M. A Digital Imaging Based Multifunctional Flame Monitoring System. *Proceedings of the 20th IEEE Instrumentation and Measurement Technology Conference*, Vail, CO, May 20–22, 2003.

- (17) Sun, D.; Lu, G.; Zhou, H.; Yan, Y. Measurement of Soot Temperature, Emissivity, and Concentration of a Heavy-Oil Flame through Pyrometric Imaging. *Proceedings of the IEEE International Instrumentation and Measurement Technology Conference*, Graz, Austria, May 13–16; 2012.
- (18) Yelverton, T. L.; Roberts, W. L. Soot surface temperature measurements in pure and diluted flames at atmospheric and elevated pressures. *Exp. Therm. Fluid Sci.* **2008**, *33*, 17–22.
- (19) Zhou, H.; Zhou, B.; Qu, H.; Lin, A.; Cen, K. Experimental Investigation of the Growth of Ash Deposits with and without Additives through a Digital Image Technique. *Energy Fuels* **2012**, *26*, 6824–6833.
- (20) Zhou, H.; Zhou, B.; Dong, K.; Ding, J.; Cen, K. Research on the Slagging Characteristics of Easy to Slagging Coal in a Pilot Scale Furnace. *Fuel* **2013**, *109*, 608–615.
- (21) Matje, R. H.; French, D.; Ward, C. R.; Pistorius, P. C.; Li, Z. Behavior of Coal Mineral Matter in Sintering and Slagging of Ash during the Gasification Process. *Fuel Process. Technol.* **2011**, *92*, 1426–1433.
- (22) Ward, C. R.; Taylor, J. C.; Matulis, C. E.; Dale, L. S. Quantification of Mineral Matter in the Argonne Premium Coals Using Interactive Rietveld-Based X-ray Diffraction. *Int. J. Coal Geol.* **2001**, *46*, 67–82.
- (23) Ward, C. R.; French, D. Determination of Glass Content and Estimation of Glass Composition in Fly Ash Using Quantitative X-ray Diffractometry. *Fuel* **2006**, *85*, 2268–2277.
- (24) Rietveld, H. M. A Profile Refinement Method for Nuclear and Magnetic Structures. *J. Appl. Crystallogr.* **1969**, *2*, 65–71.
- (25) Niu, Y.; Tan, H.; Ma, L.; Pourkashanian, M.; Liu, Z.; Wang, X.; et al. Slagging Characteristics on the Superheaters of a 12 MW Biomass-Fired Boiler. *Energy Fuels* **2010**, *24*, 5222–5227.
- (26) Zhang, J.; Zhao, Y.; Wei, C.; Yao, B.; Zheng, C. Mineralogy and Microstructure of Ash Deposits from the Zhuzhou Coal-Fired Power Plant in China. *Int. J. Coal Geol.* **2010**, *81*, 309–319.
- (27) Robinson, A.; Junker, H.; Baxter, L. Pilot-Scale Investigation of the Influence of Coal-Biomass Cofiring on Ash Deposition. *Energy Fuels* **2002**, *16*, 343–355.
- (28) Madhiyanon, T.; Sathitruangsak, P.; Sungworagarn, S.; Pipatmanomai, S.; Tia, S. A Pilot-Scale Investigation of Ash and Deposition Formation during Oil-Palm Empty-Fruit-Bunch (EFB) Combustion. *Fuel Process. Technol.* **2012**, *96*, 250–264.
- (29) Wang, H.; Qiu, P.; Shi, X.; Zhang, J.; Chen, Y.; Wu, S. Effect of Key Minerals on the Ash Melting Behavior in a Reducing Atmosphere. *Energy Fuels* **2011**, *25*, 3446–3455.